Microchemical Journal 219 (2025) 115786

Contents lists available at ScienceDirect

Microchemical Journal

journal homepage: www.elsevier.com/locate/microc

Dual-quenching driven PEC sensor based on CdS@$SnIn_4S_8$ Z-scheme core-shell heterojunction for tumor marker CA72-4 detection

Aiying Wang [a], Dehao Jia [a], Kezhen Qi [b], Yu Du [c], Yamei Li [a,*], Shuyuan Liu [b,*], Zhen Yu [a,*], Qin Wei [a,c,**], Huangxian Ju [a]

[a] Collaborative Innovation Center for Green Chemical Manufacturing and Accurate Detection, Key Laboratory of Interfacial Reaction & Sensing Analysis in Universities of Shandong, School of Chemistry and Chemical Engineering, University of Jinan, Jinan 250022, PR China
[b] College of Pharmacy, Dali University, Dali 671000, Yunnan, China
[c] Department of Chemistry, Sungkyunkwan University, Suwon 16419, Republic of Korea

ARTICLE INFO

Keywords:
Z-scheme heterojunction
Photoelectrochemical immunosensing
Dual-quenching
CdS@$SnIn_4S_8$
CA72-4

ABSTRACT

A novel photoelectrochemical (PEC) biosensor integrating a rationally designed Z-scheme heterojunction was developed for the ultrasensitive detection of the tumor biomarker CA72-4. The sensing platform was constructed by in-situ anchoring $SnIn_4S_8$ nanosheets onto CdS microstructures to form a core–shell Z-scheme heterojunction. This unique architecture significantly accelerated the separation and migration of photogenerated charge carriers while effectively suppressing electron–hole recombination, thereby generating an amplified initial photocurrent signal. Furthermore, NiO nanoparticles were employed as a PEC quenching label. They achieved a dual quenching effect by simultaneously competing with the photoactive substrate for the electron donor and attenuating the incident light. This synergistic mechanism drastically reduced the photocurrent efficiency, enabling the ultrasensitive detection of CA72-4. The fabricated biosensor demonstrated excellent selectivity and reliable reproducibility, with an inter-batch relative standard deviation of 2.3 %. A wide linear response range from 0.001 to 100 U/mL was achieved under optimized conditions, with a low detection limit of 0.00037 U/mL (S/N = 3). This research offers a robust approach for CA72-4 detection and highlights the significant potential of Z-scheme heterojunction engineering for the development of advanced PEC biosensing platforms.

1. Introduction

In the contemporary era, malignant neoplasms have emerged as a predominant threat to global health. Carbohydrate Antigen 72-4 (CA72-4), a sialylated glycoprotein biomarker, has been validated for clinical applications in gastric cancer surveillance and the differential diagnosis of ovarian malignancies [1,2]. The epidemiological trajectory of the latter has exhibited an alarming progressive escalation in age-standardized incidence rates. Therefore, the development of rapid and sensitive methods for CA72-4 detection is highly significant for early cancer detection and prognostic evaluation of therapy. Conventional detection methods, such as fluorescent immunoassays and enzyme-linked immunoassays (ELISA), are often limited by their relatively low sensitivity and operational complexity [3,4]. In current research, photoelectrochemical (PEC) immunosensors have gained prominence in analytical chemistry owing to their operational simplicity, high sensitivity and cost-effectiveness [5,6]. These advantages position them as promising candidates for applications spanning environmental monitoring, biomedical diagnostics and industrial process analysis [7–9].

Photoactive materials are essential components that function as the core of photoelectrochemical sensors. Among them, cadmium sulfide (CdS), a typical metal sulfide, has been widely employed due to its appropriate band gap (approximately 2.4 eV) and exceptional responsiveness to visible light. [10,11]. Consequently, CdS nanostructures and thin films have found extensive application as visible-light sensitizers in photocatalytic hydrogen production, organic degradation, and solar cells [12–14]. However, inherent drawbacks of CdS, including pronounced photocorrosion and rapid recombination rate of photogenerated electron-hole pairs, have impeded its broader practical applications [15–17]. To alleviate charge recombination and augment

---

* Corresponding authors.
** Corresponding author at: Collaborative Innovation Center for Green Chemical Manufacturing and Accurate Detection, Key Laboratory of Interfacial Reaction & Sensing Analysis in Universities of Shandong, School of Chemistry and Chemical Engineering, University of Jinan, Jinan 250022, PR China.
E-mail addresses: 18753681626@163.com (Y. Li), lsy_19870110@126.com (S. Liu), 022270904763@ujn.edu.cn (Z. Yu), sdjndxwq@163.com (Q. Wei).

https://doi.org/10.1016/j.microc.2025.115786
Received 20 September 2025; Received in revised form 9 October 2025; Accepted 15 October 2025

quantum efficiency, the strategic construction of heterojunctions via interfacial engineering has been demonstrated to be highly efficacious [18]. For instance, wang's team developed core@dual-shell CdS/SnS_2 heterostructures via hydrothermal epitaxial growth. This architecture improved carrier separation efficiency by optimizing the band alignment, thereby enabling ultra-sensitive detection of the ovarian cancer biomarker CA-125 via a PEC immunoassay [19]. Despite these advances, conventional type II heterojunctions remained fundamentally constrained by inadequate charge carrier separation. In contrast, Z-scheme heterojunction exhibited a unique charge-transfer pathway that effectively separates photogenerated carriers, yielding significant gains in carrier-separation efficiency [20]. Duan et al. designed a double Z-scheme heterojunction based on CdTe QDs/Bi_2MoO_6/CdS to achieve sensitive identification of circulating tumor cells (CTCs) [21]. The selection of semiconductors with complementary band structures is therefore a pivotal factor in designing efficient Z-scheme systems [22]. Among numerous candidates, $SnIn_4S_8$, a ternary chalcogenide with a cubic spinel structure, has been identified as a promising n-type semiconductor. It exhibits a narrow band gap, excellent physicochemical stability, low cost, and superior photocorrosion resistance [23,24]. The Z-scheme heterojunction, fabricated by integrating CdS and $SnIn_4S_8$, exhibits optimal energy level alignment, which facilitates the directed migration of photogenerated charge carriers. This configuration results in a significant enhancement of the photocurrent response, establishing a solid foundation for highly sensitive PEC detection.

The signal-off mode, as a classic modality of PEC immunosensors, has been widely employed due to its operational simplicity and robust stability [25]. A critical aspect of constructing such sensors is identifying an effective quenching agent with a pronounced effect. The use of p-n junction-based quenching has emerged as a prevalent strategy in PEC applications [26]. As a p-type semiconductor, nickel oxide (NiO) often formed nanostructure with a large specific surface area, which facilitated the formation of efficient and stable photocatalytic active sites [27]. The photogenerated electrons participate in oxygen reduction reactions with dissolved O_2 in the electrolyte, yielding superoxide radical anions ($\cdot O_2^-$). Under illumination, NiO nanoparticles undergo photoexcitation to generate electron-hole pairs. The photogenerated electrons participate in oxygen reduction reactions with dissolved O_2 in the electrolyte, yielded superoxide$\cdot O_2^-$ [28]. This competitive electron consumption pathway reduced the availability of the ascorbic acid (AA) electron donor at the photoanode interface, thereby diminishing the steady-state photocurrent. Owing to these favorable attributes, p-type NiO was selected in this research as an effective quencher for the n-type CdS@$SnIn_4S_8$ composite to construct a highly sensitive signal-off immunosensor.

Therefore, an innovative signal-off PEC immunosensor was developed for the ultrasensitive quantification of CA72-4. This platform was constructed using a Z-type CdS@$SnIn_4S_8$ heterojunction as a photoactive matrix and p-type NiO as an effective signal quencher. The CdS and $SnIn_4S_8$ heterojunction, synthesized via a hydrothermal method, exhibited optimal photocurrent response by significantly enhancing light absorption and promoting the separation of photogenerated charge carriers. Concurrently, the NiO quencher, with its high specific surface area, suppressed the photocurrent through a dual mechanism, competitive consumption of the electron donor and attenuation of incident light. The fabricated immunosensor demonstrated excellent performance for CA72-4 quantification, showing great promise for application in the clinical diagnosis of ovarian cancer.

2. Experimental section

2.1. Materials and instruments

Details of all reagents and instrumentation were provided in the Supplementary Material.

2.2. Synthesis of NiO nanospheres

An aliquot (0.124 g) of Nickel(II) acetate tetrahydrate ($Ni(CH_3COO)_2{\cdot}4H_2O$) was dissolved in 30 mL of 1,2-propanediol under magnetic stirring at 500 rpm. The mixture was subjected to ultrasonication treatment and then underwent hydrothermal synthesis in a Teflon-lined autoclave at 170 °C for 20 h. After cooling to room temperature, the resulting precipitate was collected by centrifugation, washed three times with ethanol, and dried under vacuum at 60 °C for 2 h. The material was calcined in a muffle furnace under static air conditions, with the temperature increased at a programmed rate of 2 °C per minute to 800 °C, followed by a 2 h holding period at this final temperature (Scheme 1A).

2.3. Synthesis of CdS@$SnIn_4S_8$

In a typical synthesis, 0.2 mmol of Stannous chloride pentahydrate ($SnCl_2{\cdot}5H_2O$) and 0.4 mmol of Indium(III) chloride tetrahydrate ($InCl_3{\cdot}4H_2O$) were dissolved in 60 mL of ethylene glycol under vigorous stirring. Thioacetamide (1 mmol) and pre-synthesized CdS (0.16 mmol) were then introduced into the homogeneous solution. The mixture was vigorously stirred and ultrasonicated for 10 min before being transferred to a Polytetrafluoroethylene (PTFE)-lined autoclave and maintained at 160 °C for 4 h under hydrothermal conditions. The autoclave was allowed to cool naturally to ambient temperature. The resulting CdS@$SnIn_4S_8$ composite was isolated via centrifugation (Scheme 1B), thoroughly rinsed with ethanol, and then dried under vacuum at 60 °C overnight [29].

2.4. Synthesis of NiO-Ab_2 bioconjugates

Firstly, 0.1 g of NiO was dispersed in a solvent system composed of 80 mL of ethanol, 20 mL of deionized water, and 1 mL of concentrated ammonia solution (128 wt%). Subsequently, 67 μL each of tetraethyl orthosilicate (TEOS) and 3-aminopropyltriethoxysilane (APTES) were introduced into the mixture. The reaction was then continuously stirred at 35 °C for 3 h to obtain aminated NiO nanoparticles (NiO-NH_2). Next, 1 mL of 10 μg/mL antibody (Ab_2) was combined with 1 mL of 2 mg/mL NiO-NH_2 and incubated with gentle shaking at 4 °C overnight. After that, the mixture was centrifuged, and the resulting precipitate was redispersed in 1 mL of 0.1 M phosphate-buffered saline (PBS, pH 7.4) to yield NiO-Ab_2.

2.5. Construction of PEC immunosensor

Initially, the indium tin oxide (ITO) glass substrates were sectioned into standardized dimensions and subjected to a preheating process. Then, 10 μL of CdS@$SnIn_4S_8$ solution (8 mg/mL) was drop-cast onto the surface of ITO electrode surface and allowed to air-dry under ambient conditions. Next, a 3 μL aliquot of 3 mM thioglycolic acid (TGA) solution was applied onto the CdS@$SnIn_4S_8$-modified electrode. Subsequently, the prepared electrodes were incubated with 3 μL of 1-ethyl-3-(3-dimethylaminopropyl) carbodiimide (EDC) and N-hydroxysuccinimide (NHS) solutions to activate the carboxylate groups. After each incubation step (TGA and EDC/NHS), the electrode was thoroughly rinsed with deionized water to remove any unbound residues. A sequential drop-casting procedure was then employed, 6 μL of 10 μg/mL Ab_1 antibody, 3 μL of 1 wt% bovine serum albumin (BSA), 6 μL of CA72-4 antigen at various concentrations, and 6 μL of a 2 mg/mL NiO-Ab_2 solution were successively deposited onto the electrode surface, with incubation at 4 °C for 1 h. Finally, the electrode was extensively washed with PBS (0.1 M, pH 7.4) and dried under ambient conditions (Scheme 1C).

2.6. Testing of PEC sensors

A typical three-electrode setup was utilized in this study, with the

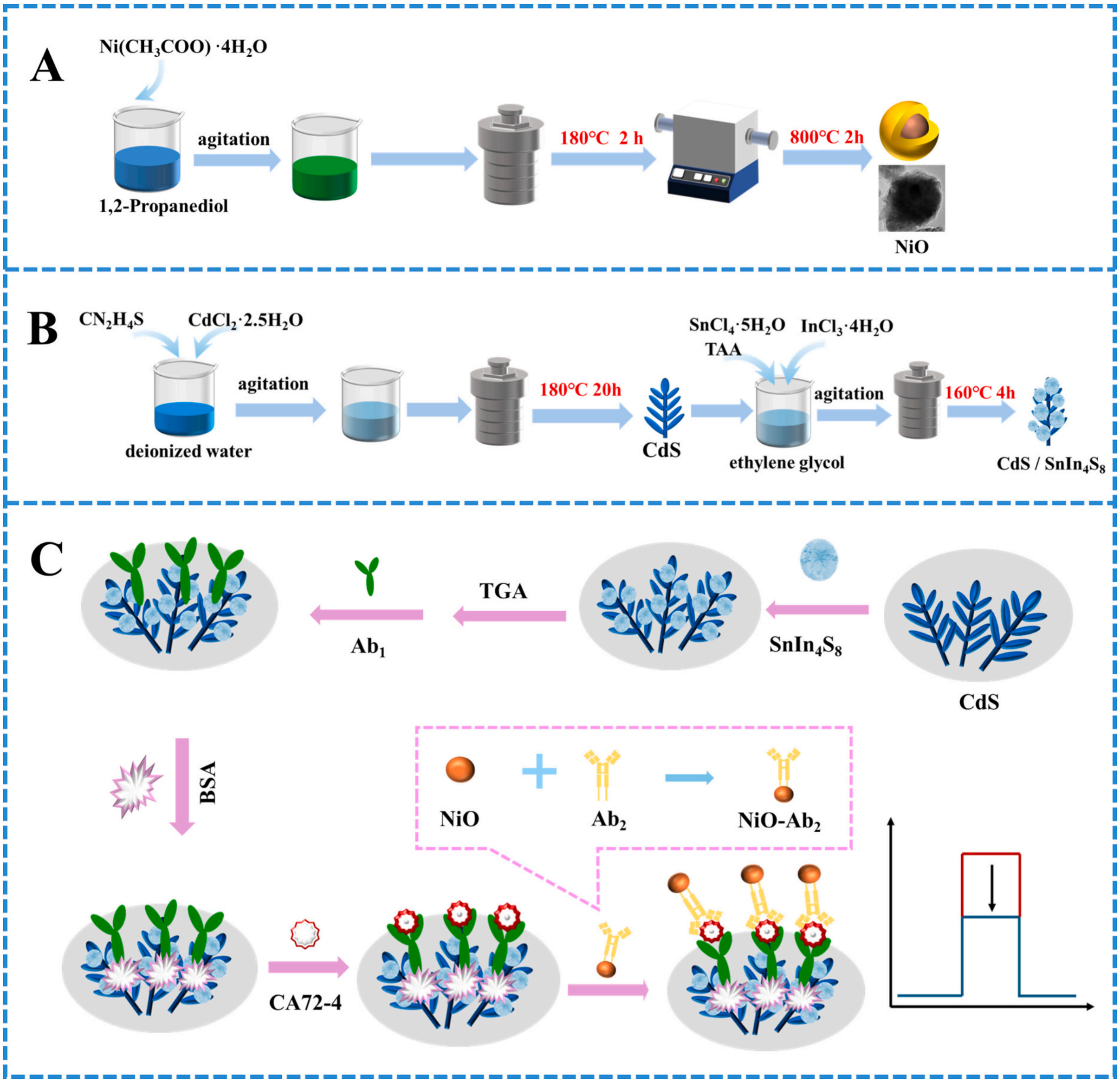

Scheme 1. (A) Preparation process of NiO and (B) CdS@$SnIn_4S_8$. (C) Schematic illustration of the signal-off PEC immunoassay system.

prepared photoelectrode, an Ag/AgCl electrode, and a platinum wire serving as the working, reference, and counter electrodes, respectively. The PEC response was recorded at 0 V in PBS (pH = 7.4) under illumination from a 100 W LED, using a CHI760E electrochemical workstation.

3. Results and discussion

3.1. Characterization of CdS@$SnIn_4S_8$, NiO

The microstructure and elemental composition of CdS, CdS@$SnIn_4S_8$ and NiO were characterized using Scanning electron microscopy (SEM), transmission electron microscopy (TEM) and X-ray diffraction (XRD). The SEM image of pure CdS powder revealed a wheat ear-like microstructure with dimensions ranging from 5 to 10 μm (Fig. 1A). As shown in Fig. 1B, pure $SnIn_4S_8$ was composed of irregular nanosheets that assembled into a micro-floral morphology. These $SnIn_4S_8$ nanosheets were tightly wrapped around the CdS surface, forming a hydrangea-like morphology (Fig. 1C). The attachment not only establishes a heterostructure with the underlying CdS but also substantially enhanced the material's specific surface area, thereby improving light absorption and photocurrent response. As shown in Fig. 1D, Elemental mapping analysis of the CdS@$SnIn_4S_8$ composite demonstrated homogeneous spatial distribution of constituent elements (Sn, In, S, and Cd). In the HRTEM micrograph, interplanar spacings of 0.27 nm and 0.35 nm were discernible, corresponding to the (007) plane of $SnIn_4S_8$ and the (002) plane of CdS (Fig. 1E). This provides clear for the successful formation of the heterojunction. TEM characterizationfurther revealed that NiO nanoparticles were irregularly spherical with diameters ranging from 100 to150 nm (Fig. 1F).

The crystalline structure and phase composition of the resulting sample confirmed by XRD. As depicted in Fig. 1G, the characteristic diffraction peaks at 25.0°, 26.6°, 28.3°, 36.8°, 43.9° and 48.0° (2θ) were assigned to the (1 0 0), (0 0 2), (1 0 1), (1 0 2), (1 1 0) (1 1 2) and (1 0 3) crystal planes of cubic phase CdS (red line), respectively [30]. The peaks observed at 9.4°, 18.7°, 28.3° and 50.0° were indexed to the (2 0 0), (2 0 2), (6 0 0) and (0 0 6) crystal planes of $SnIn_4S_8$ (black line), respectively [31]. In Fig. 1H, three additional diffraction peaks emerged at 44.5°, 51.8° and 76.3°, which belong to the (1 1 1), (2 0 0) and (2 2 0) crystal planes of rhombohedral nickel oxide (NiO) (PDF#97-016-6122), demonstrating the successful preparation of NiO nanoparticles.

To investigate the surface functionalization of NiO nanoparticles

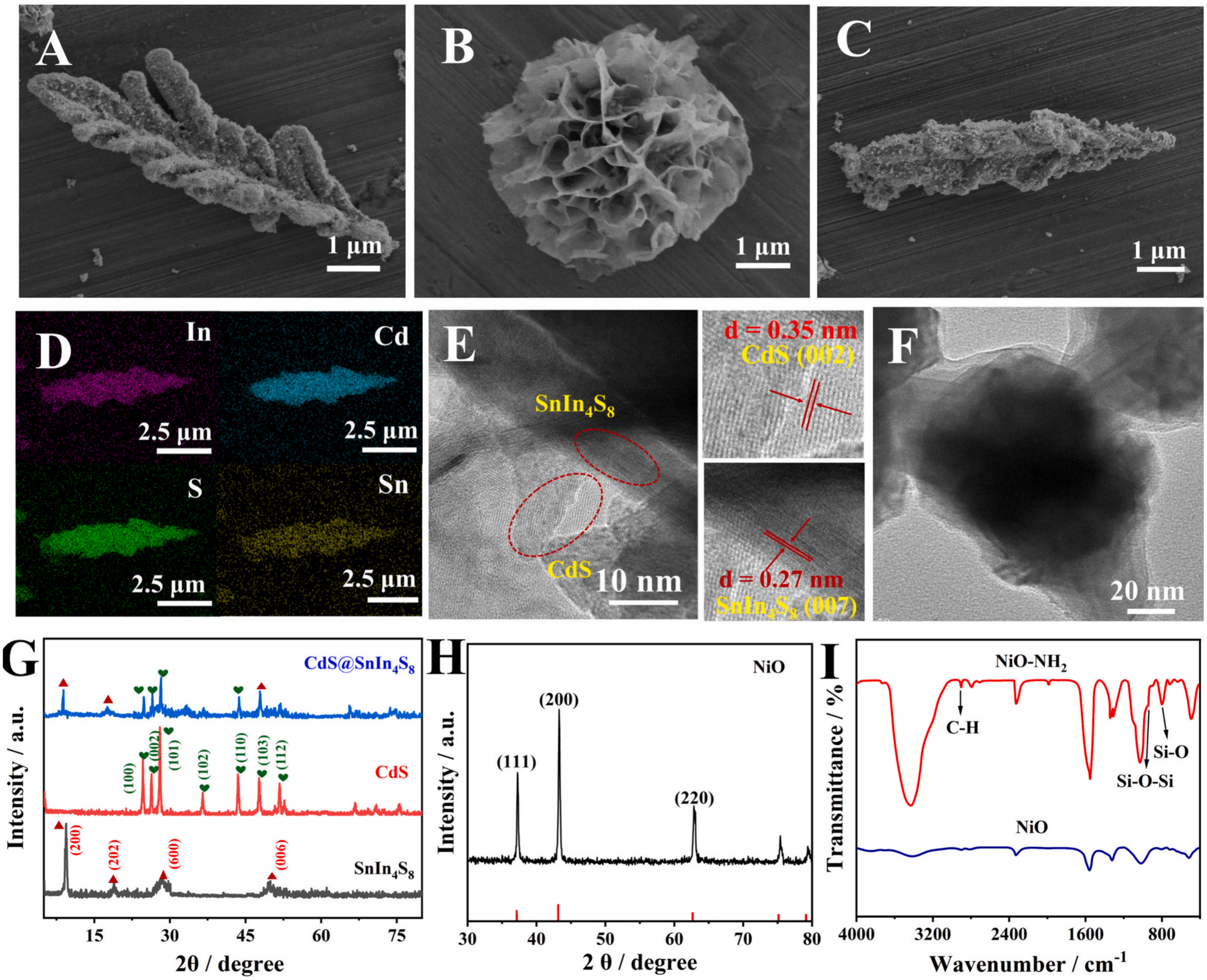

Fig. 1. SEM photographs of (A) CdS, (B) $SnIn_4S_8$ and (C) CdS@$SnIn_4S_8$. (D) Elemental mapping images of CdS@$SnIn_4S_8$ in SEM. (E) TEM image of the CdS@$SnIn_4S_8$. (F) The HRTEM image of NiO. (G) XRD pattern of $SnIn_4S_8$ (in black), CdS (in red), and CdS@$SnIn_4S_8$ (in blue). (H) XRD analysis pattern of NiO. (I) Fourier-transform infrared (FT-IR) spectra for NiO (in blue) and NiO-NH_2 (in red). (For interpretation of the references to colour in this figure legend, the reader is referred to the web version of this article.)

with aminopropyltriethoxysilane (APTES), FT-IR spectroscopy was performed. As illustrated in Fig. 1I, the APTES-functionalized NiO (NiO-NH_2) exhibited three characteristic absorption bands at 2916 cm^{-1}, 1003 cm^{-1} and 820 cm^{-1} that were absent in the pristine NiO sample. These observed bans were attributed to the vibrational modes of C—H, Si—O—Si and Si—O functional groups from APTES. This confirms the effective grafting of APTES molecules onto the NiO surface through covalent bonding, indicating successful amination of the nanoparticles.

Further confirmation of the effective formation of the CdS@$SnIn_4S_8$ composite was obtained through X-ray photoelectron spectroscopy (XPS) analysis. The survey spectrum verified the simultaneous presence of S, In, Cd and Sn elements (Fig. 2A). The high-resolution Cd 3d spectrum showed symmetric peaks at the binding energies of 405.17 eV and 411.90 eV, which is consistent with the typical spin-orbit splitting values of Cd^{2+} (Fig. 2B). As shown in Fig. 2C, the S 2p spectrum revealed a doublet at 161.4 eV and 162.4 eV, attributable to the spin-orbit components S $2p_{3/2}$ and S $2p_{1/2}$, respectively, typical of S^{2-} species in metal sulfides. Similarly, the In 3d spectrum exhibited peaks at 444.7 eV ($3d_{5/2}$) and 452.4 eV ($3d_{3/2}$), confirming the In^{3+} coordination (Fig. 2D). In the Sn 3d spectrum, two distinct peaks were observed at 486.5 eV ($3d_{5/2}$) and 494.9 eV ($3d_{3/2}$), confirming that Sn existed in the +4 oxidation state with in $SnIn_4S_8$ lattice (Fig. 2E). The XPS analysis above provides definitive evidence for the presence of CdS@$SnIn_4S_8$. Notably, a positive shift in the binding energy of Cd was observed upon composite formation, indicating a strong electronic interaction between CdS and $SnIn_4S_8$ during the hybridization process and suggesting enhanced stability of the composite (Fig. 2F). Furthermore, the electronic structure of sulfur, involving p and d orbitals, is known to facilitate electronic transitions. This, combined with the observed interfacial interaction, suggests that the CdS@$SnIn_4S_8$ heterojunction improves light utilization, thereby enhancing the overall photoelectrochemical activity. The surface elemental composition and valence states of the NiO samples were analyzed by XPS. As shown in Fig. S1A, all target elements were detected without detectable impurities. The Ni 2p spectrum was deconvoluted into four components, the main Ni $2p_{3/2}$ peak at 853.7 eV and its satellite at 862.8 eV, alongside the Ni $2p_{1/2}$ peak at 874.4 eV with its satellite at 878.7 eV, characteristic of Ni^{2+} (Fig. S1B). As shown in Fig. S1C, the O 1s spectrum was fitted with two components at 529.5 eV and 531.8 eV, attributed to lattice oxygen (O^{2-}) and surface chemisorbed oxygen species (—OH/O_2^-), respectively.

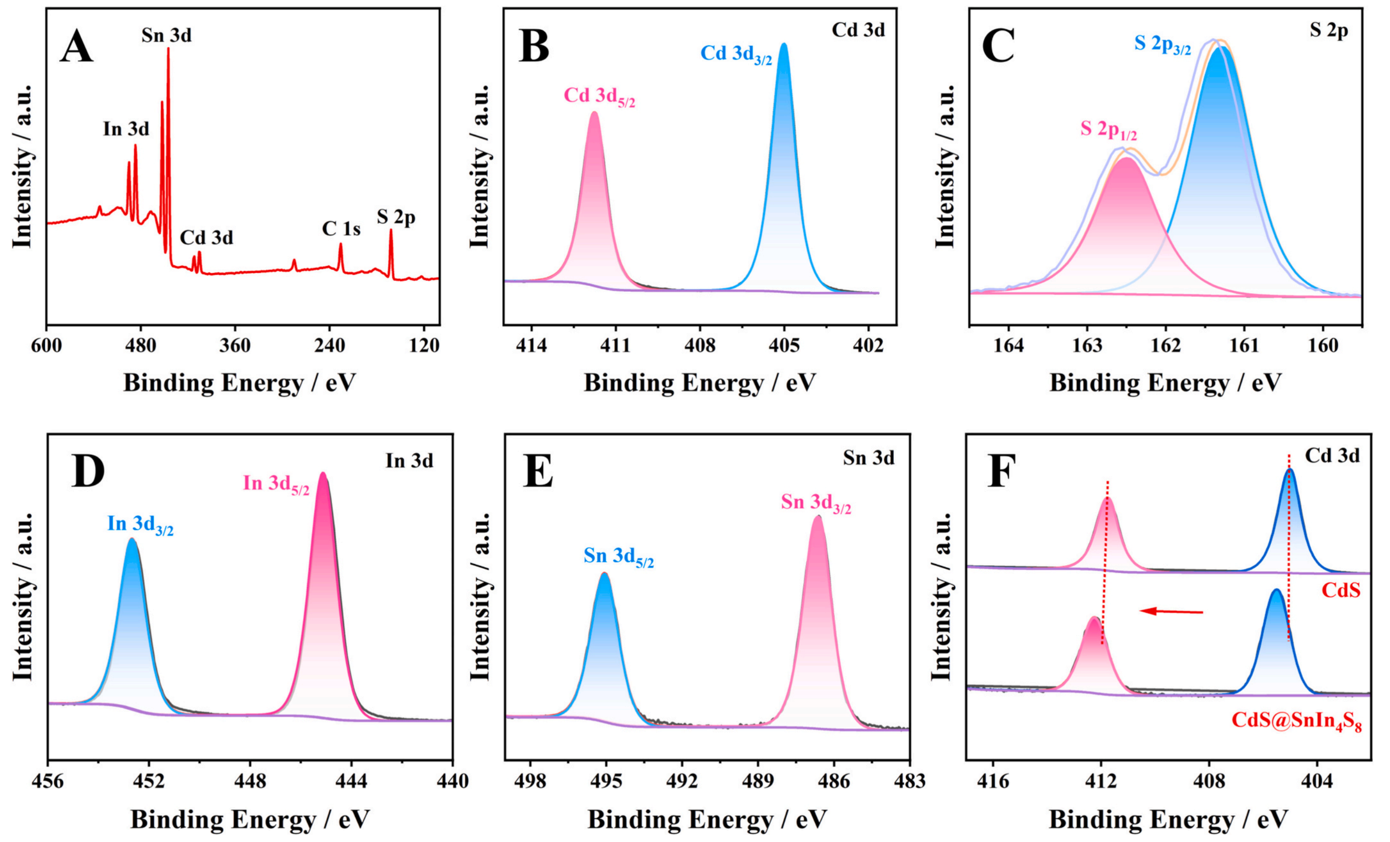

Fig. 2. XPS analysis of the CdS@$SnIn_4S_8$: (A) Full survey scan; High-resolution spectra of (B) Cd 3d, (C) S 2p, (D) In 3d and (E) Sn 2p; (F) Comparative Cd 3d spectra of $SnIn_4S_8$ and the CdS@$SnIn_4S_8$.

3.2. Discussion on the mechanism of immunosensors

UV–vis diffuse reflectance spectroscopy (DRS) was utilized to investigate the optical absorption properties of the photoactive materials [32]. As shown in Fig. S2A, the formation of CdS@$SnIn_4S_8$ resulted in a significant enhancement of visible light absorption compared to the individual CdS and $SnIn_4S_8$ components. The optical bandgap energies (E_g) of CdS, $SnIn_4S_8$ and NiO were determined to be 2.30 eV (Fig. S2B), 2.27 eV (Fig. S2C) and 2.72 eV (Fig. S2D), respectively. The Mott-Schottky (M-S) plots yielded flat band potentials (E_{fb}) of −0.93 eV and −1.05 eV (vs. Ag/AgCl) for CdS and $SnIn_4S_8$ (Fig. S2E and S2F), respectively. Using the equation E_{CB} (vs. NHE) $\approx$ E_{fb} (vs. Ag/AgCl) + 0.197 V, the conduction band (CB) potentials were calculated to be −0.73 eV and −0.85 eV (vs. NHE) for CdS and $SnIn_4S_8$. Furthermore, the valence band (VB) potentials were derived from the relation $E_{VB} = E_{CB} + E_g$, yielding values of 1.57 eV and 1.42 eV (vs. NHE), respectively. This band structure analysis revealed a staggered alignment of the energy levels between CdS and $SnIn_4S_8$, which is consistent with the characteristics of a Z-scheme heterojunction. As illustrated in Fig. 3, under light irradiation, photogenerated electrons in the conduction band of CdS recombined with photogenerated holes in the valence band of $SnIn_4S_8$ at the heterojunction interface. This charge recombination pathway facilitates the spatial separation of the remaining useful charge carriers. Furthermore, the NiO nanoparticles introduced significant steric hindrance, which impeded thet electron transfer pathways between AA molecules and the photoelectrode surface, thereby amplifying the photocurrent suppression signal. This systematic investigation elucidated the synergistic Z-scheme charge transfer dynamics and the quencher interaction mechanisms, establishing a fundamental principles for the rational design of high-performance PEC sensors.

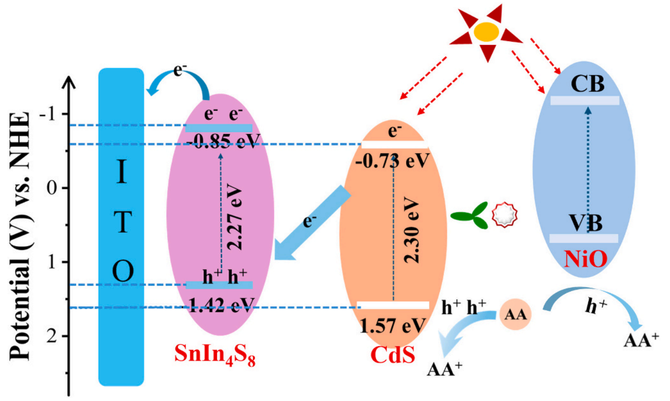

Fig. 3. Diagram of the possible mechanisms of the PEC immunosensor.

3.3. Construction of sensor

Photocurrent response analysis was employed to validate the successful stepwise construction of the PEC immunosensor [33]. As shown in Fig. 4A and Fig. S3, the bare ITO electrode (curve a) showed a negligible photocurrent. In contrast, modification with CdS@$SnIn_4S_8$ (curve b) resulted in a substantial signal enhancement. Subsequent functionalization steps, including antibody (Ab_1, curve c), BSA (curve d) and biomarker CA72-4 conjugation (curve e), induced a progressive attenuation of the photocurrent. This decrease is the most primarily attributed to the passivation effects of the insulating BSA layer and the increased steric hindrance from the assembled biomolecules, which impeded electron transfer. Notably, the introduction of the NiO-Ab_2 quencher (curve f) caused a significant reduction in the photocurrent.

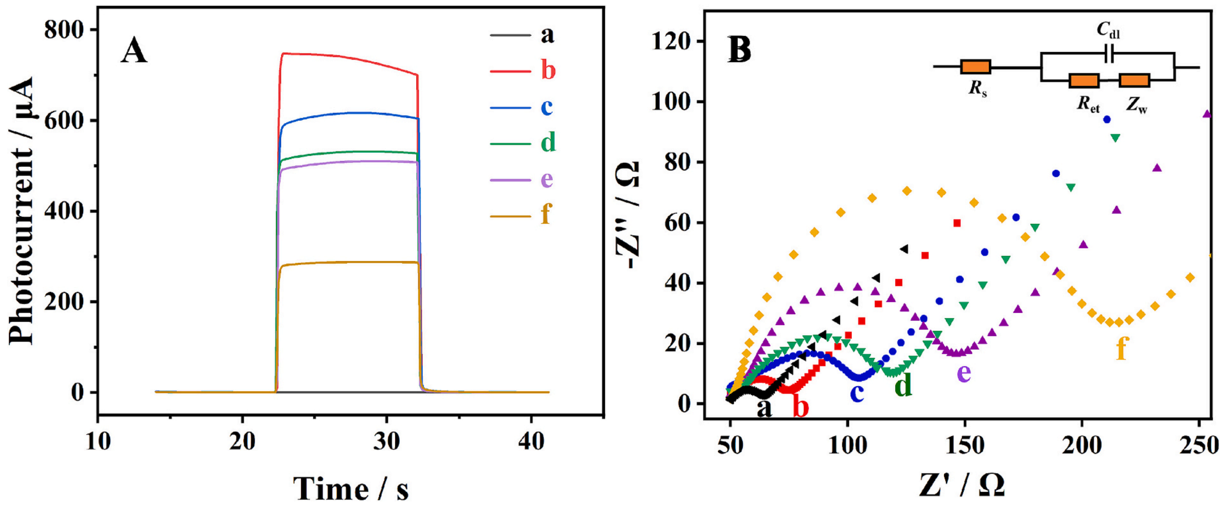

Fig. 4. (A) Photocurrent response and (B) EIS spectra corresponding to the following modified electrodes: (a) ITO, (b) ITO/CdS@$SnIn_4S_8$, (c) ITO/CdS@$SnIn_4S_8$/Ab_1, (d) ITO/CdS@$SnIn_4S_8$/Ab_1/BSA, (e) ITO/CdS@$SnIn_4S_8$/Ab_1/BSA/CA72-4, (f) ITO/ CdS@$SnIn_4S_8$/Ab_1/BSA/CA72-4/NiO-Ab_2.

This quenching effect was ascribed to the competitive light absorption by NiO and its consumption of the electron donor AA.

Electrochemical Impedance Spectroscopy (EIS) was used to further characterize the interfacial properties and electron transfer resistance (R_{et}) during the immunosensor fabrications. The R_{et} value, which correlated with the semicircle diameter in Nyquist plots, is shown in Fig. 4B and Table S1. The bare ITO electrode exhibited a very small semicircle, indicating low charge transfer resistance, which is consistent with its high conductivity. The R_{et} increased progressively with the sequential immobilization of Ab_1, BSA, CA72-4, and finally the NiO-Ab_2 complex. This stepwise increase in impedance confirms the successful assembly of the immunosenor interface, as each insulating biomolecular layer hinders electron transfer at the electrode surface.

3.4. Condition optimization and immunesensor performance

To maximize biosensing efficiency, the operational performance of the PEC immunosensor was systematically investigated and optimized under the collective influence of multiple external variables. As shown in Fig. S3A, the photocurrent initially increased and then decreased with increasing concentration of the CdS@$SnIn_4S_8$, reaching a maximum at 8 mg/mL. The effects of PBS buffer pH and AA concentration were also investigated (Fig. S3B and S3C). The photocurrent response was achieved using a PBS solution at pH 7.4 containing 0.1 mol/L AA

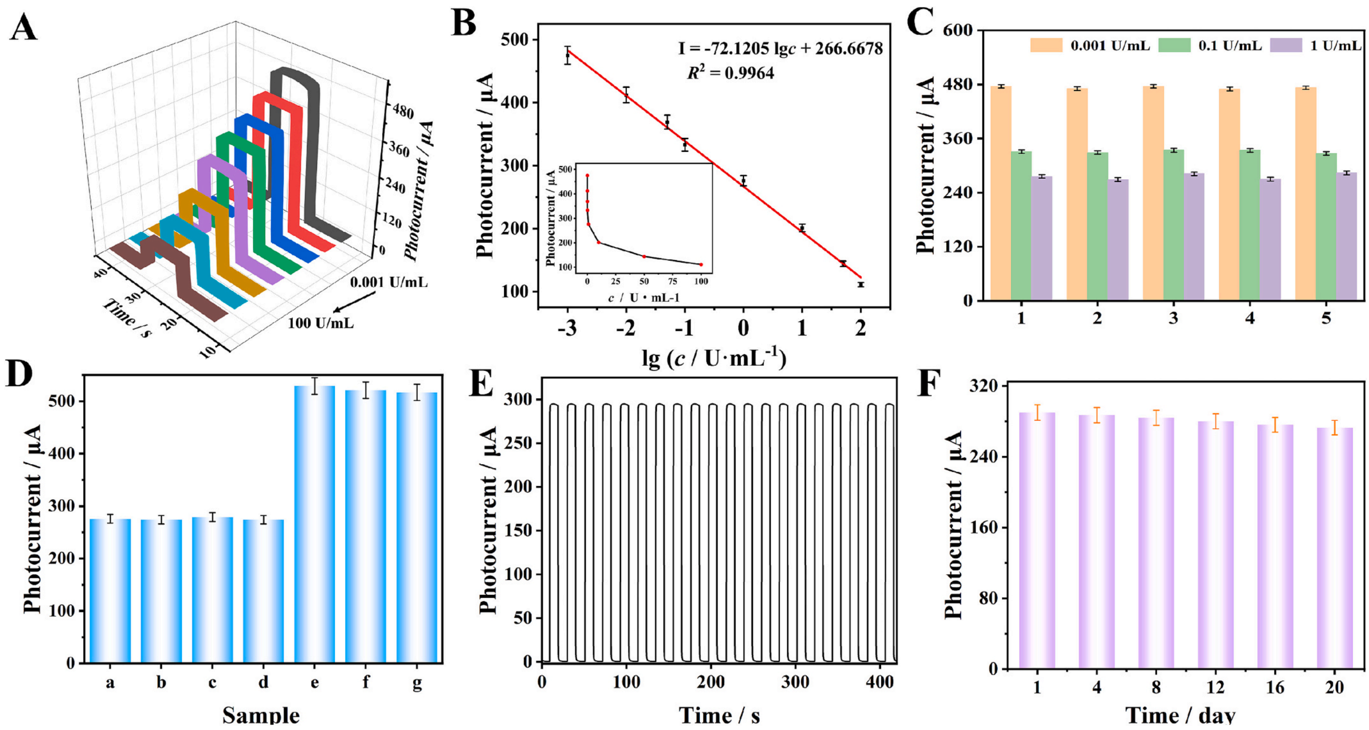

Fig. 5. (A) Photocurrent response of CdS@$SnIn_4S_8$ heterojunction for CA72-4 detection. (B) Calibration plots corresponding to various concentrations of CA72-4 ranging from 0.001 to 100 U/mL. (C) Reproducibility testing of CA72-4 concentrations by PEC sensors. (D) Specificity of the PEC immunosensor toward (a) CA72-4, (b) CA72-4 and NSE, (c) CA72-4 and CYFRA21-1, (d) CA72-4 and CEA, (e) NSE, (f) CYFRA21-1, (g) CEA. (E) The stability and (F) storage stability of the proposed PEC immunosensor.

Furthermore, a maximum PEC signal was observed at an Ab_1 incubation time of 60 min (Fig. S4D); therefore, this incubation duration was selected for all subsequent experiments.

Under these optimized conditions, the fabricated immunosensor exhibited a linear detection range for CA72-4 from 0.001 to 100 U/mL. As shown in Fig. 5A and Fig. 5B, the photocurrent intensity showed a negative correlation with the logarithm of CA72-4 concentration. The calibration curve was defined by $I = -72.1205 \lg c + 266.6678$ ($R^2 = 0.9964$), where I represented photocurrent and c denoted CA72-4 concentration. The calculated detection limit (LOD) was 0.00037 U·mL^{-1} (S/N = 3), which surpasses the performance of most reported CA72-4 immunosensors (refer to Table S2 for a comparative analysis).

3.5. *Stability, reproducibility and selectivity*

The repeatability, reproducibility and selectivity of the sensor were evaluated. To assess repeatability, five independently prepared electrodes were tested at three different CA72-4 concentrations (0.001, 0.1 and 1 U/mL). As shown in Fig. 5C, the photocurrent responses exhibited relative standard deviations ranging (RSDs) from 1.1 % to 3.1 %, indicating excellent measurement repeatability. Selectivity was evaluated by testing the response to the target analyte (0.1 U/mL CA72-4) in the presence of potentially interfering substances, including 10 ng/mL neuron-specific enolase (NSE), cytokeratin 19 fragment (CYFRA21-1), and carcinoembryonic antigen (CEA). As shown in Fig. 5D, the detection signal for CA72-4 showed almost no change compared to the signal from the pure CA72-4 sample, demonstrating high specificity. The responses to the interfering substances alone were negligible. Stability was assessed through both operational and storage tests. The operational stability was evaluated by subjecting the sensor to 20 on/off irradiation cycles (10s each). The sensor retained over >95 % of its initial photocurrent response (Fig. 5E), confirming its robust durability under continuous operation. For storage stability, the sensor was stored at 4 °C and tested periodically. After 20 days, it retained 94.1 % of its initial response, demonstrating excellent long-term stability (Fig. 5F).

3.6. *Actual sample testing*

To validate the feasibility and accuracy of the constructed biosensor, CA72-4 detection in serum was performed using the standard addition method. The human serum samples were fortified with CA72-4 at concentrations of 2.00, 5.00, 7.00 and 9.00 U/mL (Table 1). The measured recovery rates were 98.0 %, 101 % and 99.7 %, respectively, with RSD ranging from 1.1 % to 2.4 %. These findings demonstrated the biosensor's potential for clinical testing applications.

4. Conclusions

In summary, a sensitive PEC immunosensor for CA72-4 detection was constructed based on a $CdS@SnIn_4S_8$ Z-scheme heterojunction as the photoactive material and NiO as a photocurrent quencher. Systematic mechanistic studies revealed that the Z-scheme heterojunction effectively promoted the spatial separation and directional migration of photogenerated electron-hole pairs, leading to a significantly enhanced and stable photocurrent response. In addition, based on a competitive quenching mechanism, the introduction of NiO effectively regulated the photocurrent signal through competitive consumption of the electron donor and light absorption. This quenching strategy dramatically amplified the photocurrent signal change upon biomolecular binding, thereby greatly improving the detection sensitivity. The developed PEC immunosensor exhibited a wide linear range from 0.001 to 100 U/mL and a low detection limit of 0.00037 U/mL for CA72-4. Consequently, this biosensing platform demonstrated superior selectivity, reliable reproducibility and favorable stability, showing great promise for clinical biomarker analysis.

Table 1
Test results for CA72-4 in samples.

Content of CA72-4 in the serum (U/mL)	The addition content (U/mL)	The detection content (U/mL $n = 5$)	The average content (U/mL)	RSD (% n = 5)	Recovery (%)
4.78	2.00	6.63, 6.69, 6.75 6.81, 6.84	6.74	1.3	98.0
	5.00	9.74, 9.77, 9.85 9.89, 10.01	9.85	1.1	101
	7.00	11.34, 11.68, 11.83, 11.92, 12.04	11.76	2.4	99.7
	9.00	13.69, 13.94, 13.70, 13.84, 13.86	13.81	0.78	100.6

CRediT authorship contribution statement

Aiying Wang: Writing – original draft, Data curation, Conceptualization. **Dehao Jia:** Writing – review & editing, Methodology. **Kezhen Qi:** Writing – review & editing, Methodology. **Yu Du:** Writing – review & editing, Methodology. **Yamei Li:** Writing – review & editing. **Shuyuan Liu:** Writing – review & editing, Supervision. **Zhen Yu:** Writing – review & editing, Methodology. **Qin Wei:** Supervision, Project administration, Funding acquisition. **Huangxian Ju:** Writing – review & editing.

Declaration of competing interest

The authors declare that they have no known competing financial interests or personal relationships that could have appeared to influence the work reported in this paper.

Acknowledgements

This study was supported by the National Natural Science Foundation of China (22574062, 22574063), the Natural Science Foundation of Shandong Province (ZR2022QB117), the Yunnan Provincial Science and Technology Plan Project (202405AF140007), and the Taishan Scholar Young Expert of Shandong Province (tsqn202306227).

Appendix A. Supplementary data

Supplementary data to this article can be found online at https://doi.org/10.1016/j.microc.2025.115786.

Data availability

No data was used for the research described in the article.

References

[1] L.V. Bel'skaya, E.A. Sarf, A.I. Loginova, D.M. Vyushkov, E.D. Choi, Potential diagnostic value of salivary tumor markers in breast, lung and ovarian Cancer: a preliminary study, current issues, Mol. Biol. (2023) 5084–5098.
[2] A. Margoni, A.N. Gargalionis, A.G. Papavassiliou, CA-125:CA72-4 ratio – towards a promising cost-effective tool in ovarian cancer diagnosis and monitoring of post-menopausal women under hormone treatment, J. Ovarian Res. 17 (1) (2024) 164.
[3] S. Ju, Y. Xiang, Y. Xie, L. Zuo, J. Li, X. Li, Y. Wang, Q. Huang, M. Zhang, X. Wu, Y. Wang, Q. Shi, X. Hu, Virtual screening reveals fluorescent probes for detecting Pan-zinc center activity in serum MMPs: a potential biomarker for early tumor screening, Chem. Eng. J. 498 (2024) 155319.
[4] H. Yan, L. Jiao, H. Wang, W. Xu, Y. Wu, W. Gu, D. Du, Y. Lin, C. Zhu, A "sense-and-treat" ELISA using zeolitic imidazolate framework-8 as carriers for dual-modal detection of carcinoembryonic antigen, Sensors Actuators B Chem. 297 (2019) 126760.

[5] W. Chen, Z. Luo, J. Guo, L. Li, H. Wu, Photoelectrochemical immunosensing of amyloid-β peptide using nanoplasmonic macroporous bismuth vanadate for Alzheimer's disease diagnosis, Sens. Actuat. Rep. 9 (2025) 100309.

[6] Y. Cai, Z. Bi, X. Geng, J. Chi, M. Gao, Y. Liu, Z. Qiu, X. Zhang, L. Yu, Z. Chen, W. Shan, M. Qiu, Ultrasensitive CEA detection using SiO_2/AuNPs-mediated dual inhibition in a signal-off-type photoelectrochemical immunosensor, Anal. Chim. Acta 1345 (2025) 343745.

[7] S.S. Nemati, G. Dehghan, Photoelectrochemical biosensors: prospects of graphite carbon nitride-based sensors in prostate-specific antigen diagnosis, Anal. Biochem. 696 (2025) 115686.

[8] R. Nie, D. Liao, W. Yan, W. Liang, J. Zhi, Y. Guo, C. Dong, L. Fan, Design an efficient molecularly imprinted photoelectrochemical sensor for detection of butyl benzyl phthalate, Sensors Actuators B Chem. 430 (2025) 137357.

[9] J. Zhang, L. Zhao, Y. Xue, A.-J. Wang, L.-P. Mei, P. Song, J.-J. Feng, A split-type photoelectrochemical sensor based on In_2S_3/PCN-224 Z-scheme heterojunction for ultrasensitive detection of ampicillin, Microchim. Acta 192 (3) (2025) 144.

[10] Q. Huang, J. Zhang, Z. Song, X. Deng, S. Luo, W. Yuan, X. He, P. Zheng, S. Wang, L. Wang, Construction of S-type CdS@$ZnIn_2S_4$ heterojunctions with core-shell hollow nanosphere and their application in visible light photocatalytic degradation of antibiotics, J. Alloys Compd. 1020 (2025) 179492.

[11] Z. Dong, D. Li, T. Han, X. Zhao, X. Lei, Boosting solar hydrogen generation by growth of UiO-based MOF on metal sulfide surface, Environ. Chem. Eng. 13 (3) (2025) 116141.

[12] H. Li, C. Zheng, Z. Wang, Q. Xu, F. Meng, Z. Bai, W. Yue, G. Nie, Hydrazine-induced synthesis of CdS nanorings for the application in photodegradation, Res. Chem. Intermed. 49 (7) (2023) 2807–2826.

[13] Y. Ma, M. Fa, Y. Zhang, L. Xiong, X. Li, S. Zhou, W. Chen, L. Mao, A $AgPd_3$/2D-CdS photocatalyst: the function of $AgPd_3$ cocatalyst, and the enhanced photocatalytic hydrogen generation property under visible light, Int. J. Hydrog. Energy 116 (2025) 378–388.

[14] N.K. Das, S.F.U. Farhad, A.K.S. Gupta, E.M.K.I. Ahamed, M.A. Matin, N. Amin, The significance of bilayer window (CdS:O/CdS) on the performance of CdTe thin film solar cells, Opt. Mater. 155 (2024) 115816.

[15] H. Tian, Y. Li, Q. Dai, S. Wei, Z. Qiu, W. Wang, P-N heterojunction to boost photoelectrochemical H_2 evolution of CdS/$AgVO_3$ nanorod arrays photoanode, J. Power Sources 632 (2025) 236341.

[16] Y. Zakariyya, H.Y. Hafeez, J. Mohammed, C.E. Ndikilar, A.B. Suleiman, D. Umaru, Recent trends and optimization strategies for CdS-based photocatalysts: a scale-up approach for efficient solar fuel (hydrogen) generation, Int. J. Hydrog. Energy 95 (2024) 185–211.

[17] J. Zhang, E. Wu, B. Qian, M. Cai, J.-Q. Bai, Y. Jiang, J. Chen, C.-J. Mao, S. Sun, Reinforcing cd-S bonds through morphology engineering for enhanced intrinsic photocatalytic stability of CdS, J. Colloid Interface Sci. 677 (2025) 963–973.

[18] B. Zhu, W. Fu, J. Qu, T. Zhang, Z. Zhang, X. Ye, Z. Gao, G. Zhu, X. Guan, L. Guo, Ultrafast carrier dynamics triggered by Ga-S bond in GaZnON/CdS heterojunction for efficient photocatalytic hydrogen evolution, Chem. Eng. J. 497 (2024) 154712.

[19] J. Wang, J. Xie, M. Chen, S. Zheng, H. Tan, S. Yu, Y. Chen, X. Huang, W. Gao, Core-double-shell structure and heterojunction in CdS/SnS_2 boosting fast carrier separation for ultrasensitive detection of carbohydrate antigen 125, Sensors Actuators B Chem. 380 (2023) 133352.

[20] R. Kumar, A. Sudhaik, D. Kumar, R. Devi, E. Devi, A. Chawla, P. Raizada, C. M. Hussain, T. Ahamad, P. Singh, Synergistic photocatalytic activity of Bi_2O_3/g-C_3N_4/ZnO ternary heterojunction with dual Z-scheme charge transfer towards textile dye degradation, J. Ind. Eng. Chem. 144 (2025) 575–584.

[21] S. Duan, H. Zhang, Z. Liu, J. Li, L. Gao, H. Jiang, J. Wang, Photoelectrochemical and fluorescent dual-mode sensitive detection of circulating tumor cells based on aptamer DNA-linked CdTe QDs/Bi_2MoO_6/CdS "double Z-scheme" system, Talanta 292 (2025) 127922.

[22] J. Dang, J. Guo, L. Wang, F. Guo, W. Shi, Y. Li, W. Guan, Construction of Z-scheme Fe_3O_4/BiOCl/BiOI heterojunction with superior recyclability for improved photocatalytic activity towards tetracycline degradation, J. Alloys Compd. 893 (2022) 162251.

[23] L. Huang, Y. Wang, K. Deng, X. Sun, X. Li, Y. Xie, P. Zhao, J. Fei, In-situ growth of flower-like $CdIn_2S_4$ on three-dimensional microspheres SnIn4S8 to form S-scheme heterojunction for efficient detection of tert-butylhydroquinone in edible oils, Chem. Eng. J. 509 (2025) 161413.

[24] C.-H. Shen, Y. Chen, X.-J. Xu, X.-Y. Li, X.-J. Wen, Z.-T. Liu, R. Xing, H. Guo, Z.-H. Fei, Efficient photocatalytic H_2 evolution and Cr(VI) reduction under visible light using a novel Z-scheme $SnIn_4S_8$/CeO_2 heterojunction photocatalysts, J. Hazard. Mater. 416 (2021) 126217.

[25] C. Ye, Z. Wu, K. Ma, Z. Xia, J. Pan, M. Wang, C. Ye, Ti_3C_2 MXene-based Schottky photocathode for enhanced photoelectrochemical sensing, J. Alloys Compd. 859 (2021) 157787.

[26] M.-J. Li, Y.-N. Zheng, W.-B. Liang, R. Yuan, Y.-Q. Chai, Using p-type PbS quantum dots to quench photocurrent of fullerene–au NP@MoS_2 composite structure for ultrasensitive Photoelectrochemical detection of ATP, ACS Appl. Mater. Interfaces 9 (48) (2017) 42111–42120.

[27] W. Wang, W. Zhang, C. Hao, F. Wu, Y. Liang, H. Shi, J. Wang, T. Zhang, Y. Hua, Enhanced photoelectrochemical activity and photocatalytic water oxidation of NiO nanoparticle-decorated $SrTiO_3$ nanocube heterostructures: interaction, interfacial charge transfer and enhanced mechanism, Sol. Energy Mater. Sol. Cells 152 (2016) 1–9.

[28] K. Zhu, S.K. Frehan, G. Mul, A. Huijser, Dual role of surface hydroxyl groups in the Photodynamics and performance of NiO-based photocathodes, J. Am. Chem. Soc. 144 (24) (2022) 11010–11018.

[29] S. Zhang, B. Zhang, Y. Jiang, Y. Xiao, W. Zhang, H. Xu, X. Yang, Z. Liu, J. Zhang, In-situ constructing of one-dimensional $SnIn_4S_8$-CdS core-shell heterostructure as a direct Z-scheme photocatalyst with enhanced photocatalytic oxidation and reduction capabilities, Appl. Surf. Sci. 542 (2021) 148618.

[30] L. Chang, G. Zhu, H. Lu, M. Hojamberdiev, Z. Zhang, J. Gao, C. Wang, W. Yang, In situ formation of leaf-like Ag_2S/CdS heterojunction Photocatalyst harnessing Vis–NIR light for Photodegradation of organic pollutants, Catal. Lett. 148 (9) (2018) 2765–2776.

[31] Y. Zhang, J. Chen, H. Wang, Q. Cui, D. Fan, Y. Zhang, X. Ren, H. Ma, Q. Wei, H. Ju, Novel Photoelectrochemical biosensing platform based on a double type II $CdLa_2S_4$/$SnIn_4S_8$/Sb_2S_3 ternary heterojunction as photoactive materials and $NiCo_2O_4$ Nanospheres as a Photoquencher for CA19-9 detection, Anal. Chem. 94 (45) (2022) 15915–15923.

[32] Y. Hao, Y. Zhang, X. Zhu, J. Chen, N. Song, H. Wang, N. Zhang, D. Fan, H. Ma, Q. Wei, H. Ju, A novel photoelectrochemical biosensing platform utilizing dual type-II Bi_2O_3/$CdLa_2S_4$/Bi_2S_3 ternary heterojunctions as signal transduction materials and Cu_2O nanosphere as a sensitizer for CA15-3 detection, Chem. Eng. J. 489 (2024) 151141.

[33] J. Zhang, X. Xue, Y. Du, J. Zhao, H. Ma, X. Ren, Q. Wei, H. Ju, Antigen-down PEC Immunosensor for CYFRA21-1 detection based on photocurrent polarity switching strategy, Anal. Chem. 94 (36) (2022) 12368–12373.